Energy Technology
Generation, Conversion, Storage, Distribution
www.entechnol.de

Hybrid Anodes of Lithium Titanium Oxide and Carbon Onions for Lithium-Ion and Sodium-Ion Energy Storage

*Hwirim Shim, Stefanie Arnold, Öznil Budak, Maike Ulbricht, Pattarachai Srimuk, and Volker Presser**

This study demonstrates the hybridization of $Li_4Ti_5O_{12}$ (LTO) with different types of carbon onions synthesized from nanodiamonds. The carbon onions mixed with a $Li_4Ti_5O_x$ precursor for sol–gel synthesis. These hybrid materials are tested as anodes for both lithium-ion battery (LIB) and sodium-ion battery (SIB). Electrochemical characterization for LIB application is carried out using 1 M $LiPF_6$ in a 1:1 (by volume) ethylene carbonate and dimethyl carbonate as the electrolyte. For lithium-ion intercalation, LTO hybridized with carbon onions from the inert-gas route achieves an excellent electrochemical performance of 188 mAh g^{-1} at 10 mA g^{-1}, which maintains 100 mAh g^{-1} at 1 A g^{-1} and has a cycling stability of 96% of initial capacity after 400 cycles, thereby outperforming both neat LTO and LTO with onions obtained via vacuum treatment. The performance of the best-performing hybrid material (LTO with carbon onions from argon annealing) in an SIB is tested, using 1 M $NaClO_4$ in ethylene/dimethyl/fluoroethylene carbonate (19:19:2 by mass) as the electrolyte. A maximum capacity of 102 mAh g^{-1} for the SIB system is obtained, with a capacity retention of 96% after 500 cycles.

1. Introduction

The increased demand for energy storage applications in daily life necessitates the development of faster and more long-lasting energy storage devices. Lithium-ion batteries (LIBs) have been widely explored and implemented for mobile or stationary devices owing to their lightweight and high energy and power density.[1] Conventional LIBs use graphite as an anode due to its high theoretical capacity (372 mAh g^{-1}), good cycling stability, and natural abundance.[2] However, graphite electrodes experience major safety issues, because their operation potential is near to the lithium electroplating potential of 0.1 V versus Li/Li^+, which leads to a high risk of penetrable dendrite formation.[3,4] An alternative to graphite anodes is lithium titanium oxide ($Li_4Ti_5O_{12}$, LTO), for which good structural stability during lithiation/delithiation and safety due to its high operation potential have been reported.[5] The theoretical capacity of LTO is 175 mAh g^{-1}, utilizing three Li^+ ions via Equation (1)[6]

$$Li_4Ti_5O_{12} + 3Li^+ + 3e^- \rightarrow Li_7Ti_5O_{12} \quad (1)$$

The operation potential of the LTO range of around 1.55 V versus Li/Li^+ for Li^+ intercalation and deintercalation prevents solid electrolyte interface (SEI) formation.[7,8] In addition, LTO exhibits minor to zero volume change during operation, yielding good cycling performance, and high coulombic efficiency.[7,9] However, LTO is known for its low Li^+ ion diffusion (10^{-13}–10^{-9} cm^2 s^{-1})[10] and low electrical conductivity of 10^{-8}–10^{-13} S cm^{-1}, which limits the achievable rate capability.[11–14] The performance of LTO can be enhanced by improving the intrinsic conductivity, which can be done by the introduction of oxygen deficiencies; however, this approach requires an extra step of thermal treatment of the active material.[15] Therefore, the mechanical or chemical implementation of carbon as a conductive additive is more preferred.[16] Much work has addressed the performance by forming nanocomposite or hybridizing conductive carbon materials to LTO. The former, nanocomposites, is the most common way of producing LTO-based electrodes, usually by the use of carbon black, carbon nanotubes, or graphene.[17–20] Hybrid materials can be obtained by methods, such as surface modification of LTO by carbon coating using carbon sources, such as sucrose, glucose, solvents, acids, or gases, which have resulted in enhanced electrochemical performance.[21–25] These works document the great importance of achieving a homogenous distribution of conductive and active material on a sub-100 nm length scale.[26] Therefore, the use of synthesis methods capable of yielding nanoscale hybridization is important, especially when using nanoscale carbon additive particles.

In addition to the ability to reversibly intercalate lithium, LTO has also been demonstrated to be suitable anode in sodium-ion

H. Shim, S. Arnold, Ö. Budak, M. Ulbricht, Dr. P. Srimuk, Prof. V. Presser
Program Division Energy Materials
INM—Leibniz Institute for New Materials
Saarbrücken 66123, Germany
E-mail: volker.presser@leibniz-inm.de

H. Shim, S. Arnold, Ö. Budak, M. Ulbricht, Prof. V. Presser
Department of Materials Science and Engineering
Saarland University
Saarbrücken 66123, Germany

The ORCID identification number(s) for the author(s) of this article can be found under https://doi.org/10.1002/ente.202000679.

DOI: 10.1002/ente.202000679

batteries (SIBs).[27–34] Interest in SIBs is based on the high natural abundance of sodium and associated reduced costs.[33] The insertion–extraction potential of sodium into LTO is reported to be around 0.9 V versus Na/Na^+ without sodium metal plating on the electrode surface.[27,29,32]

The low intrinsic conductivity issue remains and possibly relates to the high overpotential or poor rate capability.[33,35] The theoretical Na^+ ion uptake capacity of LTO is also 175 mAh g^{-1}, assuming the insertion of three Na^+ ions, according to Equation (2)[27]

$$2Li_4Ti_5O_{12} + 6Na^+ + 6e^- \rightarrow Li_7Ti_5O_{12} + LiNa_6Ti_5O_{12} \quad (2)$$

In this study, we explore hybrid materials composed of sol–gel-derived LTO and nanoscale carbon onions (OLC) for use as LIB and SIB anode material. To obtain carbon onions, we used thermal annealing of nanodiamond precursors in an inert atmosphere or under vacuum to yield carbon onions with a primary particle size of 5–10 nm.[36,37] We chose carbon onions, because the absence of inner porosity and the mesopore-dominate interparticle pore space allows a highly favorable nanoscale implementation of metal oxides.[38,39] The resulting hybrid materials were electrochemically surveyed for charge storage capacity, rate capability, and cycling stability for the reversible intercalation of lithium and sodium.

2. Experimental Section

2.1. Material Preparation

Two types of carbon onions were synthesized by thermal annealing of nanodiamond powder (ND; NaBond Technologies) at 1700 °C for 1 h under Ar atmosphere, noted OLCa, or at 1300 °C for 4 h under vacuum, labeled OLCv, using high-temperature graphite furnace (Carbolite).

For the synthesis of the hybrid LTO, we used sol–gel synthesis. Lithium ethoxide dissolved in tetrahydrofuran (LiOEt, THF; Sigma Aldrich) and titanium isopropoxide (TTIP; Sigma Aldrich) were used as lithium and titanium sources, respectively. LiOEt (4 mL) was added to 5 mL of THF with vigorous stirring; then, 1.48 mL of TTIP was added dropwise to the stirring solution. Subsequently, 0.45 g of oxalic acid was added, and then, the precursor solution was stirred for 2 h at 50 °C. Appropriate amounts of OLCa or OLCv powders were added by wet impregnation into prepared sol. The carbon content was 15 mass% of the final hybrid material. The impregnated mixtures were dried at 50 °C under vacuum for overnight, followed by further drying at 80 °C for 12 h.

In addition to LTO-carbon hybrids, we also synthesized neat LTO. The latter was prepared by following the same synthesis protocol but without the addition of carbon onions. The well-dried materials were then annealed at 700 °C for 2 h (heating rate 1 °C min^{-1}) under Ar atmosphere.

The resulting materials are named "LTO" = neat LTO, "LTO-OLCa" = LTO with the addition of argon-annealed carbon onions, and "LTO-OLCv" = LTO with the addition of vacuum-treated carbon onions.

2.2. Material Characterization

2.2.1. Structural Characterization

X-ray diffraction (XRD) was carried out in a D8 Discover Diffractometer (Bruker AXS) with a copper X-ray source (Cu-K_α radiation, 40 kV, 40 mA). We used a Göbel mirror with a 1 mm point focus and a 2D X-ray detector (VANTEC-500) for the measurements. The samples were placed on a sapphire single crystal and measured with the detector being placed at angles from 20θ to 80θ with a step width of 20θ and a measuring time of 1000 s per step.

The carbon content of the hybrid materials was determined with thermogravimetric analysis (TGA), performed with a TG-209-1 Libra (Netzsch). For each TGA measurement, the samples were heated to 1000 °C under synthetic air condition (80 vol% N_2, 20 vol% O_2) with a flow rate of 20 sccm at a heating rate of 5 °C min^{-1}.

Raman spectroscopy was performed with a Renishaw inVia Raman Microscope using an neodymium-doped yttrium aluminum garnet laser with an excitation wavelength of 532 nm and a power of about 0.5 mW at the focal point. The acquisition time for each spectrum was 30 s with ten accumulations to enhance the signal-to-noise ratio. Peak fitting of the measured spectra was accomplished, assuming two Voigt peaks for the D- and G-modes individually.

Transmission electron microscopy (TEM) was performed using a JEOL 2100F system at an operating voltage at 200 kV. Samples for TEM imaging were prepared by dispersion and tip-sonication of the hybrid materials in ethanol and subsequent drop-casting of the dispersion on a copper grid with a lacey carbon film.

Scanning electron microscopy (SEM) of the prepared electrodes was conducted with a JEOL JSM-7500F system at an acceleration voltage of 3 kV and an emission current of 10 μA. The energy-dispersive X-ray spectroscopy (EDX) was carried out using an X-Max-150 detector (Oxford Instruments) attached to the SEM system. The spectra were obtained at an acceleration voltage of 15 kV and an emission current of 10 μA. Before the spectral acquisition of each sample, calibration was conducted with a silicon wafer.

The porosity of the powder materials was analyzed by the use of nitrogen gas sorption at −196 °C with an Autosorb iQ system from Quantachrome (now: Anton-Paar). The powder samples were outgassed at 300 °C for 20 h before the measurement, and the recorded gas sorption isotherms along with the calculated Brunauer–Emmett–Teller (BET) surface area values are provided in Figure S1, Supporting Information.

2.2.2. Electrochemical Characterization

For the preparation of the anode, the synthesized LTO and the hybrid materials were mixed with polyvinylidene fluoride (PVDF; Alfa Aesar) binder with a 9:1 mass ratio without any further conductivity additive, followed by the addition of *N*-methyl-2-pyrrolidone (NMP; Sigma Aldrich) solvent. The mixed slurry was coated on a copper foil (25 μm, MTI) using a 200 μm doctor blade. The coated electrode was dried overnight in a fume hood at room temperature, then transferred to a vacuum oven, and dried

at 110 °C overnight. The dried coating was pressed in a hot roll press machine (MTI), and then punched to 10 mm discs using press punch (EL-CELL) for electrochemical benchmarking. The mass loadings of each electrode were 5.5 ± 0.4 mg cm^{-2} for neat LTO 3.7 ± 0.2 mg cm^{-2} for LTO-OLCa, and 3.7 ± 0.4 mg cm^{-2} for LTO-OLCv. The dry thickness of the prepared electrode was 36 µm for neat LTO and 39 µm for the two hybrid samples. The electrode density was 1.48 g cm^{-3} for neat LTO, 0.94 g cm^{-3} for LTO-OLCa, and 0.93 g cm^{-3} for LTO-OLCv.

For half-cell measurements, an LTO containing working electrode and lithium or a sodium disc counter and reference electrodes were assembled into CR2032 coin cells. We used a Whatman GF/F glass fiber separator and 1 M $LiPF_6$ salt in a mixture of ethylene carbonate and dimethyl carbonate (EC:DMC; 1:1 by volume, Sigma Aldrich) or 1 M $NaClO_4$ in a mixture of EC:DMC with 5 mass% fluoroethylene carbonate (FEC) as the electrolyte.[40]

Cyclic voltammetry was carried out with a Biologic VMP300 potentiostat/galvanostat and performed in a potential window from 1.0 to 2.8 V versus Li/Li$^+$ and 0.3 to 2.5 V versus Na/Na$^+$ at the scan rates of 0.1–10 mV s^{-1}. Electrochemical impedance spectroscopy (EIS) was measured at an applied AC voltage amplitude of 10 mV from the frequency range of 10^6–10^{-2} Hz. For quantifying the rate handling capability, galvanostatic charge/discharge with potential limitation (GCPL) measurement was carried out at an Arbin Battery Cycler in a potential range of 1.0–2.8 V versus Li/Li$^+$ and 0.3–2.5 V versus Na/Na$^+$ using specific currents ranging from 0.01 to 10 A g^{-1} and 0.025 to 5 A g^{-1}, respectively. The cycling stability was quantified using GCPL at a specific current of 0.1 A g^{-1} for both LIB and SIB testing. All the measurements were carried out in climate chambers (Binder) set to 25 ± 1 °C.

The specific capacity C_{sp} of the hybrid material was calculated by integration of the applied lithium or sodium extraction current I over the extraction time t accounting for the deintercalation step from 1.0 to 2.8 V versus Li/Li$^+$ and 0.3 to 2.5 V versus Na/Na$^+$, as in Equation (3)

$$C_{sp} = \frac{\int_{t_0}^{t} I dt}{m} \tag{3}$$

The specific capacity was normalized to the total mass of the hybrid material m in the electrode without the polymer binder.

3. Results and Discussion

3.1. Hybrid Material Synthesis

Figure 1A presents the schematic illustration of the LTO-OLC hybrid. The preparation of LTO sols and wet impregnation of two different types of carbon onions synthesized under different conditions lead to a synthesis of the hybrid material LTO-OLCa and LTO-OLCv by thermal annealing. As shown in TEM images (Figure 1B–D), LTO, LTO-OLCa, and LTO-OLCv show nanoscale crystalline domains related to lithium-titanium oxide. For better comparison, TEM images of carbon onions (OLCa and OLCv) are presented in Figure S2A,B, Supporting Information.

XRD was used to determine and study the crystal structure of the prepared pristine and hybrid materials. The data of all X-ray diffractograms (**Figure 2**A) match very well to cubic spinel lithium titanium oxide (LTO, PDF 49-0207, $a = 8.359$ Å). The measurement data are dominated by signals from the crystalline LTO phase, whereas the contribution of the incompletely graphitic carbon is mostly lost in the background; more information on the carbon structure can be inferred from the Raman spectra (later paragraph). We used Rietveld refinement to calculate the average coherence length (roughly corresponding with the domain size) of LTO (Table S1, Supporting Information). All sample materials, that is, LTO and the two types of LTO-carbon

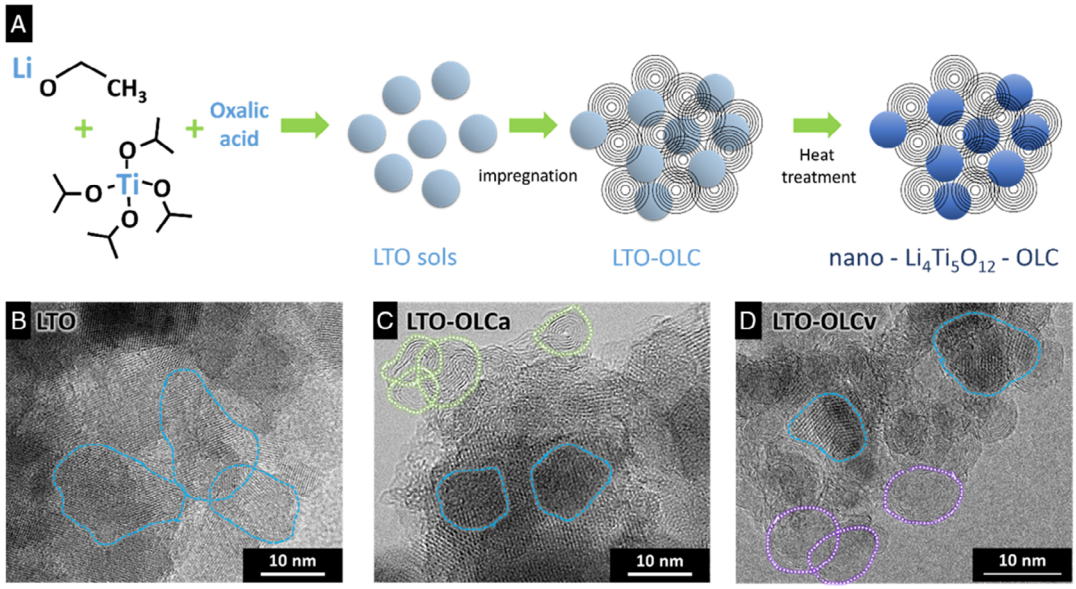

Figure 1. A) Schematic illustration of preparation for hybrid nano-LTO-OLC. The transmission micrograms of B) LTO, C) LTO-OLCa, and D) LTO-OLCv hybrid material. LTO domains are marked by blue dashed lines and carbon onions with C) green and D) purple dotted lines.

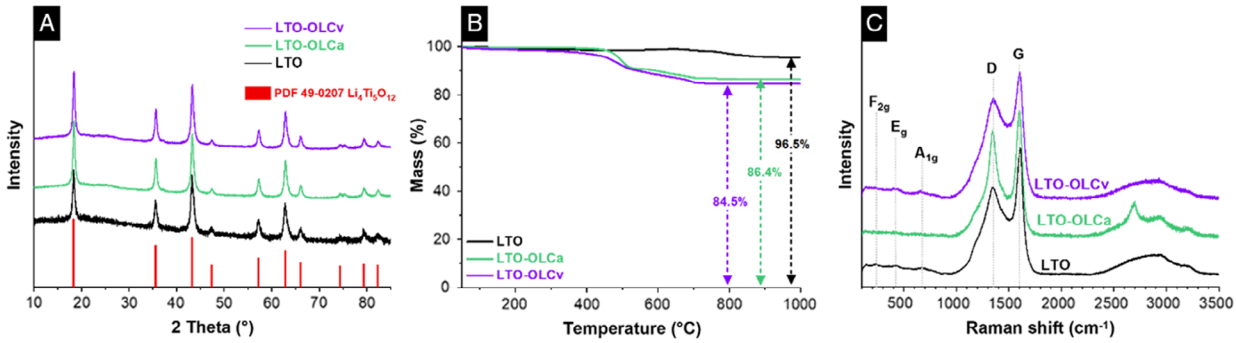

Figure 2. A) XRD patterns of LTO, LTO-OLCa, and LTO-OLCv. B) TGA of samples under synthetic air atmosphere for the characterization of the amount of carbon. C) Background-corrected Raman spectra of LTO, LTO-OLCa, and LTO-OLCv. All data were normalized to the intensity of the carbon G-mode as 100% and the intensity at 3500 cm^{-1} as 0%.

hybrids, have a highly comparable domain size of about 30 ± 2 nm and a unit cell constant of $a = 8.366 \pm 0.002$ Å.

The carbon content of the synthesized LTO hybrid materials was determined by TGA (recorded in synthetic air) and elemental (CHNS/O) analysis. As displayed in Figure 2B, LTO without carbon onions showed 3.5 mass% carbon content, which is the carbon formed during the thermal annealing of the as-prepared oxide sols from the residual chains from metal alkoxide precursors. LTO-OLCa and LTO-OLCv showed 14 and 15.5 mass% carbon content, respectively. These data agree with the carbon amount introduced during the synthesis step, and the elemental analysis results in Table S2, Supporting Information.

We characterized the carbon structure of the samples with Raman spectroscopy. The resulting spectra are presented in Figure 2C for LTO and the hybrid materials, and in Figure S2D, Supporting Information, for carbon onions. For comparison, the peak position and full-width at half-maximum (FWHM) of each D- and G-modes and the I_D/I_G ratio by use of four Voigt peak fitting are provided in Table S3, Supporting Information. The individual deconvolution of the Voigt peak fitting is presented in Figure S3, Supporting Information. The Raman spectra of all carbon onions and hybrid materials show the characteristic D-mode and G-mode of incompletely graphitized carbon (nanocrystalline carbon) and the corresponding overtones.[41] Carbon onions synthesized under argon atmosphere and vacuum show very different Raman spectra in agreement with previous studies.[36,37] Specifically, we see narrower D- and G-modes in the case of OLCa (D-mode: 71 cm^{-1}; G-mode: 70 cm^{-1}) compared with OLCv (D-mode: 176 cm^{-1}; G-mode: 90 cm^{-1}); this aligns with the much lower synthesis temperature during vacuum annealing (1300 °C) compared with the thermal treatment in argon (1700 °C). Higher synthesis temperatures are known to result in a higher order of structural ordering of the carbon phase.[42]

In Figure 2C, at lower Raman shift, characteristic vibration bands at 243, 431, and 670 cm^{-1} for LTO are observed for LTO, LTO-OLCa, and LTO-OLCv.[43–45] At first, it may be surprising to see carbon-related Raman signals for the LTO sample where no carbon onions were introduced during the synthesis. Still, we see clearly, for LTO, a D-band at 1345 cm^{-1} and a G-band at 1607 cm^{-1}. In addition, there is also the transpolyacetylene (TPA) peak in the range of 1150–1200 cm^{-1}, which indicates the highly disordered nature of carbon.[41] This carbon species is related to the carbonization of the metal alkoxide residues used for the synthesis. A small amount of carbon also aligns with the thermogram (Figure 2B), as indicated by the mass loss of about 3.5 mass% when heating above 600 °C. The presence of incompletely graphitic carbon in LTO-OLCa and LTO-OLCv is associated mostly with the carbon onions type OLCa and OLCv, respectively. We can understand the Raman spectra of LTO-OLCv and LTO-OLCa as a superimposition of the carbon seen already in the LTO sample in addition to carbon from the carbon onion structure (Figure S3D,E, Supporting Information). LTO-OLCa, compared with the other materials, shows a shaper D-mode (92 cm^{-1}) and a sharper peak of the carbon-related combination and overtone modes between 2300 and 3400 cm^{-1}. This suggests that the carbon network in LTO-OLCa, in general, possesses a higher degree of graphitic ordering compared with that of the other materials.

3.2. Lithium-Ion Intercalation Behavior and Performance

The synthesized LTO and hybrid materials were prepared to electrodes and tested with a CR2032 coin cell for electrochemical benchmarking of LIB systems. The SEM images of the prepared electrodes are found in Figure S4, Supporting Information. For an overview of the electrochemical performance, the prepared cells were first tested for cyclic voltammetry (CV) in the potential range of 1.0–2.8 V versus Li/Li^+ at various scan rates of 0.1–10 mV s^{-1}. The resulting cyclic voltammograms of LTO-OLCa are shown in **Figure 3**A, and voltammograms of LTO and LTO-OLCv are shown in Figure S5A,B, Supporting Information. For comparison, the cyclic voltammograms, which were normalized to the conducted scan rates, are also prepared and presented in Figure 3B for LTO-OLCa, and in Figure S5C,D, Supporting Information, for LTO and LTO-OLCv. In Figure 3A, the lithiation peak starts from 1.55 V versus Li/Li^+, and the delithiation peak at 1.6 V versus Li/Li^+. The peak separation is larger for faster scan rates due to the overpotential caused by kinetic limitation (Figure 3B).

For a better understanding of the charge transfer kinetics, we used Equation (4)[46–48]

$$i = av^b \tag{4}$$

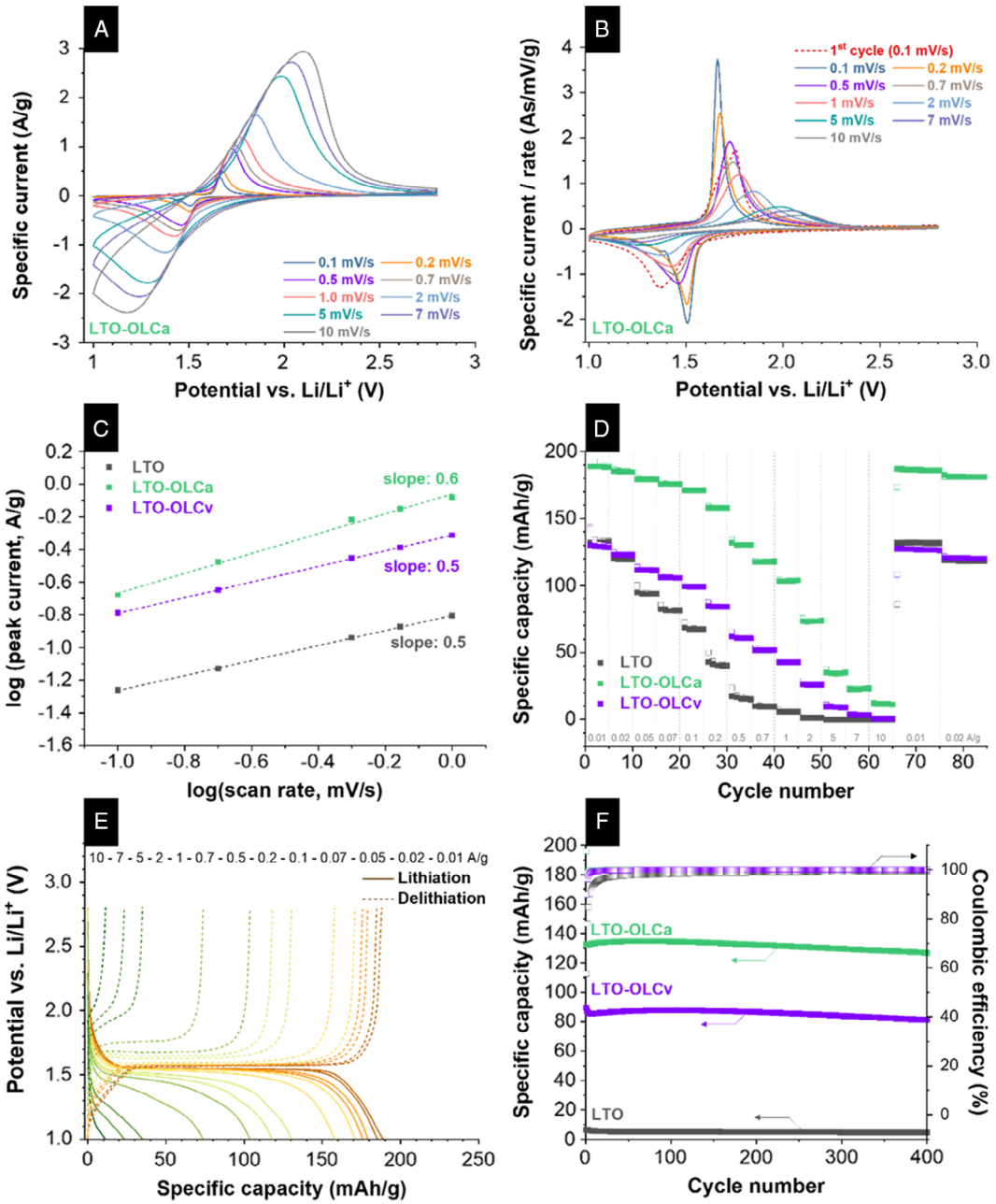

Figure 3. Lithium-ion intercalation behavior of LTO and LTO/carbon onion hybrid materials. A) Cyclic voltammograms recorded at 0.1–10 mV s^{-1} of LTO-OLCa and B) the cyclic voltammograms normalized to the recorded scan rate. C) Plot of log(*scan rate*) versus log(*peak current*) of the lithiation (cathodic) in the potential range of 1.0–2.8 V versus Li/Li^+ and the linear fitting of each sample. D) The lithiation and delithiation specific capacity of LTO, LTO-OLCa, and LTO-OLCv from galvanostatic charge/discharge cycling at different specific current for rate capability. E) Galvanostatic charge–discharge profiles of the fifth cycle at 0.01–10 A g^{-1} of sample LTO-OLCa between 1.0 and 2.8 V versus Li/Li^+. F) Galvanostatic charge/discharge cycling performance stability at a specific current of 0.1 A g^{-1} for LTO, LTO-OLCa, and LTO-OLCv.

where a and b are the variables, i is the peak specific current (A/g), and v is the scan rate (mV s^{-1}). From the obtained b value, the process kinetics fall between the boundary set by diffusion control ($b = 0.5$) or surface control ($b = 1$).[48] Figure 3C is obtained using CV data and the (shift-adjusted) peak currents of the hybrid materials at the scan rates of 0.1–1 mV s^{-1}. Thereby, we observed the b values of LTO (0.5), LTO-OLCa (0.6), and LTO-OLCv (0.5). These values are all close to the ideal case of diffusion-controlled kinetics.

To further understand the behavior of the LTO-OLC hybrids, the electrochemical impedance was measured from the prepared cells before the CV measurement, and the corresponding Nyquist plot is shown in Figure S6, Supporting Information. The spectra before the CV of LTO-OLCa and

LTO-OLCv are similar, and the spectrum of LTO is shifted toward larger resistance values. To quantify the resistance dependency on the surface reaction or charge transfer, we used the equivalent circuit of $(R_s + \mathrm{CPE1}/R_{int} + \mathrm{CPE2}/(R_{ct} + W))$, as summarized in Table S4, Supporting Information. Therein, R_s stands for the electrolyte and cell component resistance, R_{int} stands for the film formation on the interface of electrode–electrolyte, and R_{ct} stands for the charge-transfer resistance; W demarks the Warburg impedance, and CPE is a constant phase element. The high-frequency region is known to represent the contributions of the electronic resistance of the cell.[49] The charge transfer resistance of LTO before the CV (3871 Ω) is higher than the hybrid LTO-OLCa (736 Ω) and LTO-OLCv (1607 Ω), which aligns with the superior rate capability of LTO-OLCa. The contribution of R_s is negligible for LTO-OLCa (4.6 Ω) and LTO-OLCv (2.2 Ω), but very high for LTO (84.0 Ω) before CV. The integrated semi-circles indicate the resistance of surface reactions, including the electrode–electrolyte interface and the ionic mobility at the surface of the electrode.[49,50]

The rate capability of the LTO-OLC hybrid materials was tested with the GCPL technique applying specific currents between 0.01 and 10 A g^{-1} at an operational potential of 1.0–2.8 V versus Li/Li^+ (Figure 3D). The highest specific capacity of 188 mAh g^{-1} was obtained from LTO-OLCa, with a coulombic efficiency of 92%, followed by ≈130 mAh g^{-1} for LTO and LTO-OLCv, with a coulombic efficiency of ≈92%. The coulombic efficiency of LTO-OLCa further increased to ≈100% by the third cycle and maintained over 98% during the rate capability testing sequence. As the applied specific current increases above 0.5 A g^{-1}, the specific capacity of LTO-OLCa decreased with a greater margin than at smaller specific currents. The specific capacity was 11 mAh g^{-1} at a specific current of 10 A g^{-1}, and the material recovered 98.9% of the initial capacity (corresponding with 186 mAh g^{-1}) when returning to a rate of 0.01 A g^{-1}.

The LTO and LTO-OLCa displayed the same initial capacity. LTO without carbon showed a low rate capability, enabling a charge storage of only 13 mAh g^{-1} at 0.7 A g^{-1}. Furthermore, LTO recovered 99% of the initial capacity, which corresponds with 127 mAh g^{-1} when returning to a rate of 0.01 mA g^{-1}. With only 3 mass% carbon content of the LTO electrode, the electron transfer might have enough time to establish the diffusion pathway at a low current of 0.01 mA g^{-1} to obtain the specific capacity of 130 mAh g^{-1}. However, at higher specific currents that require faster transport, the LTO only demonstrated inferior rate capability. Although LTO-OLCv had the same initial capacity as the LTO, whereby LTO-OLCv showed better rate handling performance, which we ascribe to the higher carbon content of LTO-OLCv. Figure 3E shows the corresponding specific capacity and potential profile of LTO-OLCa. In good agreement with the cyclic voltammogram, the difference in the plateau between the lithiation and de-lithiation is small at low specific current (0.01–0.05 A g^{-1}). As the specific current increases, such a difference in lithiation and de-lithiation potential increases.

For comparison, the capacity and potential plot of LTO and LTO-OLCv are shown in Figure S5E,F, Supporting Information. We observed the same behavior of potential separation that the pristine LTO exhibits large potential separation already at 0.1 A g^{-1}, whereas LTO-OLCa and LTO-OLCv exhibit a large potential separation at 0.5 A g^{-1}. As the kinetic analysis suggests that diffusion is the limiting factor, the different rate handling performance (Figure 3D) must be the influence of the added OLC. Yet, the degree of graphitization carbon in LTO-OLCa is significantly better than LTO-OLCv (confirmed by Raman result, Table S3, Supporting Information). Also, the impedance data indicate better charge transport in LTO-OLCa compared with LTO-OLCv, which supports the higher lithium storage performance of LTO-OLCa. Thus, charge transfer in LTO-OLCa is faster than LTO-OLCv. The cycling performance of the LTO and LTO-OLC hybrid materials was carried out at 0.1 A g^{-1}, and the results are presented in Figure 3F, including their coulombic efficiencies. LTO-OLCa exhibits an initial capacity of 132 mAh g^{-1}, and 95.8% of the capacity remained after 400 cycles, losing only 0.013 mAh g^{-1} per cycle. Similarly, LTO-OLCv showed a slight decrease of 3 mAh g^{-1} after the initial capacity of 98 mAh g^{-1}, and then maintained 90.8% of the initial capacity.

Table 1 presents previously reported performance values of LTO/C composite and hybrid materials in comparison with data from this study. The best-performing material from our present study was LTO-OLCa material with a specific capacity of 184 mAh g^{-1} at 0.11C. The capacity retention is comparable to the state-of-the-art performance, which shows its potential as anode material for LIBs.

3.3. Sodium-Ion Intercalation Behavior and Performance

For testing the electrochemical performance for sodium-ion intercalation, we selected only LTO-OLCa due to its best

Table 1. Comparison of electrochemical performance of previously reported LTO materials with various synthesis methods and our LTO-OLCa hybrid material for LIBs.

Material	Synthesis	Specific capacity	Rate capability	Cycling stability	Reference
LTO-carbon onion	Sol–gel 700 °C, 2 h	184 mAh g^{-1} at 0.11 C	74 mAh g^{-1} at 11 C	95.8% after 400 cycles	This work
$Li_4T_5O_{12}$/C	Solid state 900 °C, 20 h	165 mAh g^{-1} at 0.2 C	–	–	[24]
Mesoporous $Li_4T_5O_{12}$/C	Self-assembly 700 °C, 2 h	144 mAh g^{-1} at 1 C	90 mAh g^{-1} at 5 C	90% after 500 cycles	[51]
$Li_4T_5O_{12}$/graphene oxide	Solid-state ball milling 500 °C, 4 h	170 mAh g^{-1} at 1 C	122 mAh g^{-1} at 30 C	94.8% after 300 cycles	[52]
$Li_4T_5O_{12}$-AC nanotubes	Electrospinning 800 °C, 3 h	120 mAh g^{-1} at 100 mA g^{-1}	84 mAh g^{-1} at 4 A g^{-1}	67% after 100 cycles	[17]
$Li_4T_5O_{12}$ porous monolith	Sol–gel, hydrothermal 700 °C, 2 h	165 mAh g^{-1} at 0.1 C	105 mAh g^{-1} at 30 C	98% after 500 cycles	[53]
$Li_4T_5O_{12}$ thin nanosheet	Hydrothermal, 600 °C, 3 h	168 mAh g^{-1} at 0.2 C	130 mAh g^{-1} at 64 C	96% after 400 cycles	[33]

performance and stability based on the LIB data. We prepared CR2032 coin cells using sodium metal as a counter and reference electrode for the electrochemical testing. Cyclic voltammetry was conducted in a potential range of 0.3–2.5 V versus Na/Na^+. **Figure 4**A presents the first and fifth voltammetric cycles at the scan rates of 0.1–10 mV s^{-1}. The first cycle shows sodiation peaks alongside the FEC redox activity starting from 0.6 V versus Na/Na^+, and the lowest current was observed at ≈0.3 V versus Na/Na^+ (Figure S7, Supporting Information). This can be ascribed to the structural change of the LTO spinel from intercalating the larger sized Na^+ ions into the interstitial sites.[29] From the next cycle, the paired sodiation/desodiation peak is observed at 0.7 and 1.05 V versus Na/Na^+, and the peak separation is enhanced, as the scan rate increases; ΔV was 0.35 V at the initial scan rate of 0.1 mV s^{-1}, 0.65 V with 0.5 mV s^{-1}, and more than 0.9 V at 1 mV s^{-1}. The higher peak separation indicates the need for higher overpotential or energy to insert/extract Na^+ ion into or out of the structure.[20]

The sodiation regime from voltammetry starts to deteriorate above with a scan rate of 2 mV s^{-1}, and at 5 mV s^{-1} and higher

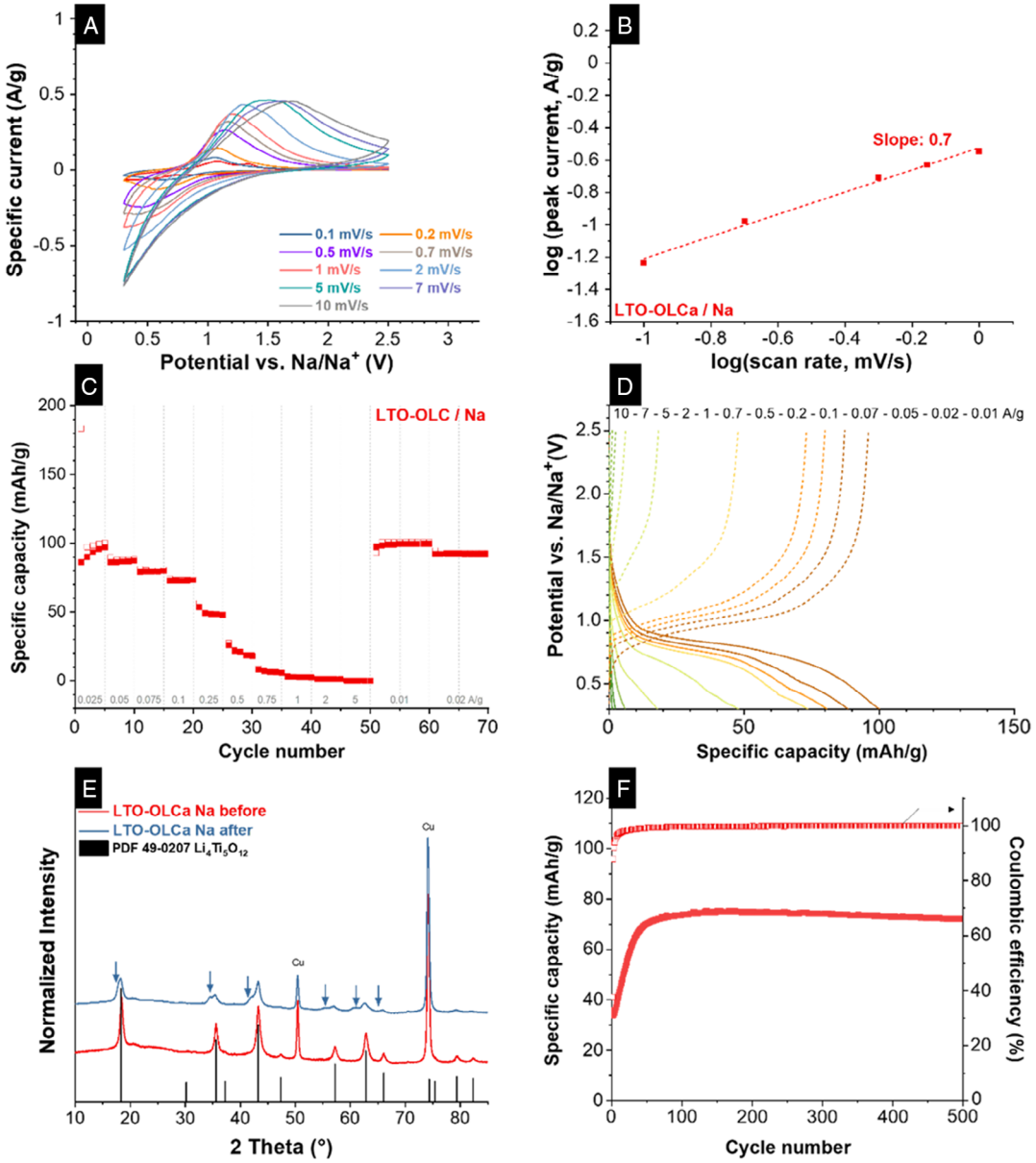

Figure 4. Sodium-ion intercalation performance of LTO-OLCa. A) Cyclic voltammograms recorded at 0.1–10 mV s^{-1} in the potential range of 0.3–2.5 V versus Na/Na^+. B) Plot of log(*scan rate*) versus log(*peak current*) of the sodiation (cathodic) in the potential range of 0.3–2.5 V versus Na/Na^+ and the linear fitting of LTO-OLCa. C) The sodiation and desodiation specific capacity of LTO-OLCa sample obtained from galvanostatic charge/discharge cycling at different specific current for rate capability. D) Galvanostatic charge–discharge profiles of the fifth cycle at 0.025–5 A g^{-1} of sample LTO-OLCa between 0.3 and 2.5 V versus Na/Na^+. E) The X-ray diffractograms of LTO-OLCa electrodes, before and after the galvanostatic charge–discharge process. F) Galvanostatic charge/discharge cycling performance stability at a specific current of 0.1 A g^{-1} for LTO-OLCa.

scan rates, the cyclic voltammograms do not show a further change in current reflex with changing scan rate. This implies that the insertion of Na^+ ion into the sites is kinetically hindered.[20] Just like for the Li-containing electrolyte, we calculated *b* values for SIB data (Figure 4B). The *b* value of LTO-OLCa tested against sodium was 0.7, which is higher than the values obtained from the lithium intercalation testing. The lowest peak current at $0.1\ mV\ s^{-1}$ scan demonstrates a significant influence on the reconstruction of the LTO structure with sodiation. The *b* value of the sodium intercalation, excluding the peak current at $0.1\ mV\ s^{-1}$, was 0.6, which is close to the value found from LIB testing.

The GCPL of the LTO-OLCa hybrid material was tested in the specific current range of 0.025–5 $A\ g^{-1}$ to quantify the rate capability. Figure 4C displays both sodiation and desodiation capacities of LTO-OLCa. The capacity values were normalized to the metal oxide mass for a better comparison with the literature. At $0.025\ A\ g^{-1}$, the initial desodiation capacity reaches $87\ mAh\ g^{-1}$ at a low coulombic efficiency of 47%. Such a low coulombic efficiency might result from the irreversible sodiation in the first cycle and the side reactions regarding SEI formation.[54] However, the desodiation capacity increases slightly from the first cycle to the fifth, which may be due to the reconstruction of the LTO structure during the insertion/extraction of the sodium ions. Accordingly, the coulombic efficiency further enhances as the cell continues being tested. Above a specific current of $0.25\ A\ g^{-1}$, the capacity decreases severely, leading to no significant insertion/extraction capacity of Na^+ above $1\ A\ g^{-1}$. To distinguish the contribution of the carbon onion, an electrode of only carbon onion annealed in Ar (OLCa) was prepared and tested with GCPL at the same operational potential and specific current. The sodiation capacity values of OLCa are presented in Figure S8B, Supporting Information, with the highest capacity of $14\ mAh\ g^{-1}$; in addition, Figure S8A, Supporting Information, displays the capacity values of OLCa when used as an LIB anode. Figure 4D shows the corresponding potential profiles of the GCPL results at the fifth cycles of each applied specific currents tested in the potential range of 0.3–2.5 V versus Na/Na^+. At lower specific currents, the Na^+ insertion into LTO begins from 0.9 V versus Na/Na^+ to 0.6 V versus Na/Na^+ with the first slope, and then continues with a different slope to 0.3 V versus Na/Na^+. When comparing the GCPL result of LTO-OLCa between lithium-ion and sodium-ion cells, one can observe the difference between the slope of the plateau (Figure 3E and 4D) suggesting higher overpotential.

To characterize possible structural change that we suspect from the first voltammetric cycles and very low coulombic efficiency of GCPL at the first cycle, we carried out post-mortem XRD analysis of the tested electrodes. The diffractograms of the electrodes before and after GCPL testing are presented in Figure 4E. The diffractogram of LTO-OLCa before cycling matches the peak position of cubic LTO, which has $a = 8.366 \pm 0.002$ Å. In addition to the set of reflection peaks inherent to LTO, we also see the emergence of another set of the same number of reflections shifted toward larger *d* values (i.e., lower scattering angles) for the LTO-OLCa after cycling. We also see sharp and intense peaks relating to the current collector material (i.e., copper). After electrochemical testing, there is a significant increase in the unit cell dimension to $a = 8.4677$ Å and a decrease in the domain size to about 10 nm. We see double peaks for the main reflections of LTO-OLCa, which indicate the coexistence of a population of LTO domains with increased unit cell volume and one close to the initial value ($a = 8.3608$ Å). This phase also has a domain size of about 10 nm, and the mass ratio between both crystallographically distinct LTO phases is about 1:1 (46:54; i.e., there is slightly less expanded LTO). The presence of about 54 mass% of residual $Na_6LiTi_5O_{12}$ is in contrast to the full electrochemical desodiation treatment of the post-mortem electrode. In agreement with previous work, when inserting Na^+ into the LTO structure, Na^+ substitutes Li in the LTO lattice. Subsequently, $Na_6LiTi_5O_{12}$ heterogeneously emerges from the LTO phase.[55] Therefore, the inability to revert all of the sodiated materials to the initial crystal structure aligns with the reduced achievable charge storage capacity of about $100\ mAh\ g^{-1}$ and the low initial coulombic efficiency of ≈50%. The disassembly of the cell was done after the desodiation step of the GCPL test; therefore, it is evident that the permanent transformation of the Na-containing phase occurs during the first cycles, as CV and GCPL profiles indicate.[34]

The size difference of Na^+ and Li^+ ions (ionic radius, $Na^+ = 102$ pm, $Li^+ = 76$ pm) is expected to trigger the poor rate performance of LTO as an anode in SIB than LIB. This size difference is initiated by the structural change, leading to more reduced cycling stability of the SIB.[29,33] Moreover, the dependency of SIB performance on the size of LTO was reported by Yu et al.,[30] which showed that smaller LTO particles enhance the rate and cycling performance of SIB. As our LTO-OLCa has a crystalline size of around 30 nm, the higher performance was expected. As presented in **Table 2**, the rate performance of LTO-OLCa in the SIB setup was not comparable to the

Table 2. Comparison of electrochemical performance of previously reported LTO materials with various synthesis methods and our LTO-OLCa hybrid material for SIBs, normalized to metal oxide mass. "rGO" means "reduced graphene oxide".

Material	Synthesis	Potential range	Specific capacity	Rate capability	Cycling stability	Reference
LTO-carbon onion	Sol–gel 700 °C, 2 h	2.5–0.3 V	97 mAh g^{-1} at 0.15 C	27 mAh g^{-1} at 2.8 C	95.6% after 500 cycles	This work
$Li_4T_5O_{12}$	Solid state 800 °C, 20 h	3.0–0.3 V	187 mAh g^{-1} at 0.1 C	–	–	[27]
Porous $Li_4T_5O_{12}$/C	Spray drying 950 °C, 24 h	3.0–0.5 V	155 mAh g^{-1} at 0.1 C	90 mAh g^{-1} at 5 C	95% after 20 cycles	[29]
$Li_4T_5O_{12}$/C nanowire	Hydrothermal 750 °C, 6 h	2.5–0.3 V	168 mAh g^{-1} at 0.2 C	38 mAh g^{-1} at 100 C	97% after 50 cycles	[31]
$Li_4T_5O_{12}$ porous monolith	Sol–gel, hydrothermal 700 °C, 2 h	1.5–0.5 V	127 mAh g^{-1} at 1 C	63 mAh g^{-1} at 30 C	70% after 100 cycles	[53]
$Li_4T_5O_{12}$ thin nanosheet	Hydrothermal, 600 °C, 3 h	2.5–0.5 V	170 mAh g^{-1} at 0.2 C	115 mAh g^{-1} at 30 C	92% after 150 cycles	[33]
$Li_4T_5O_{12}$–TiO_2/rGO aerogel	Hydrothermal 700 °C, 6 h	2.5–0.3 V	184 mAh g^{-1} at 0.5 C	77 mAh g^{-1} at 20 C	64% after 700 cycle	[56]

reported state of the art. Yet, around 96% capacity retention after 500 cycles compared with the maximum capacity is superior to the cycling performance in the reported literature, which reports very low counts of cycles. This suggests that the hybridization of LTO with carbon onion benefits the longevity of SIB (Figure 4F). Recently, Pfeifer et al. reported the importance of the appropriate selection of electrolytes for SIB application using sodium metal.[57] To enhance the performance and stability of hard carbon or sodium metal anodes for SIB, FEC was introduced to the electrolyte system additives.[54] Some have reported LTO as an anode for SIB using FEC-containing electrolytes, such as $NaClO_4$ in ethylene carbonate:diethyl carbonate:fluoroethylene carbonate (50:50:1 by volume)[58] or $NaClO_4$ in propylene carbonate:fluoroethylene carbonate (98:2 by volume),[31] which showed enhanced stability performance.

4. Conclusion

In conclusion, we synthesized nano-sized LTO and carbon onion hybrid materials and applied them, for the first time, as an anode in LIBs and SIBs. The LTO-OLCa successfully demonstrated its excellent performance with a high specific capacity of 188 mAh g^{-1} and a favorable rate capability of 74 mAh g^{-1} at 2 A g^{-1}, with 99% retention of its initial capacity after the testing to 10 A g^{-1}. The longevity test of LTO-OLCa yielded 95.8% of initial capacity, superior to both LTO synthesized without carbon onions with inferior performance, or LTO hybridized with OLCv, which only performed 91% recovery in both capacity and the retention for LIB. The LTO-OLCa, which had excellent performance in the LIB system, exhibited unsatisfactory performance when applied as anode for SIB with a specific capacity of only 102 mAh g^{-1}. Nevertheless, the longevity of LTO-OLCa with sodium showed 96% of the maximum capacity retention after 500 cycles using 1 M $NaClO_4$ in EC:DMC (1:1 by mass) containing 5 mass% FEC as the electrolyte. This work demonstrates carbon onion as a preferable hybridization substance. We believe that our LTO and carbon onion hybrid material has a potential for further improvement, for example, by the implementation of a different electrode design or a different electrolyte system to increase performance or longevity.

Supporting Information

Supporting Information is available from the Wiley Online Library or from the author.

Acknowledgements

The authors acknowledge funding from the German Federal Ministry for Economic Affairs and Energy (BMWi) in support of the HyBaCap project (award number 03ET6113C). They thank Eduard Arzt (INM) for his continuing support and Roland Bennewitz (INM) & Wiebke Buhrow (INM) for discussions and additional experimentation. Open access funding enabled and organized by Projekt DEAL.

Conflict of Interest

The authors declare no conflict of interest.

Keywords

lithium titanate, lithium titanium oxide, lithium-ion batteries, $Li_4Ti_5O_{12}$, sodium-ion batteries

Received: July 24, 2020
Revised: August 30, 2020
Published online: September 18, 2020

[1] M. Armand, J. M. Tarascon, *Nature* **2008**, *451*, 652.
[2] J. Shim, K. A. Striebel, *J. Power Sources* **2003**, *119–121*, 955.
[3] R. Yazami, P. Touzain, *J. Power Sources* **1983**, *9*, 365.
[4] R. Yazami, *Electrochim. Acta* **1999**, *45*, 87.
[5] P. Cicconi, L. Postacchini, E. Pallotta, A. Monteriù, M. Prist, M. Bevilacqua, M. Germani, *J. Power Sources* **2019**, *436*, 226837.
[6] L. Kavan, M. Grätzel, *Solid State Lett.* **2002**, *5*, A39.
[7] T. Ohzuku, A. Ueda, N. Yamamoto, *J. Electrochem. Soc.* **1995**, *142*, 1431.
[8] S. S. Zhang, K. Xu, T. R. Jow, *J. Power Sources* **2004**, *130*, 281.
[9] W. J. H. Borghols, M. Wagemaker, U. Lafont, E. M. Kelder, F. M. Mulder, *J. Am. Chem. Soc.* **2009**, *131*, 17786.
[10] B.-N. Yun, H. L. Du, J.-Y. Hwang, H.-G. Jung, Y.-K. Sun, *J. Mater. Chem.* **2017**, *5*, 2802.
[11] K. Zaghib, M. Simoneau, M. Armand, M. Gauthier, *J. Power Sources* **1999**, *81–82*, 300.
[12] S. Bach, J. P. Pereira-Ramos, N. Baffier, *J. Power Sources* **1999**, *81–82*, 273.
[13] Y. H. Rho, K. Kanamura, *J. Solid State Chem.* **2004**, *177*, 2094.
[14] B. Yan, M. Li, X. Li, Z. Bai, J. Yang, D. Xiong, D. Li, *J. Mater. Chem. A* **2015**, *3*, 11773.
[15] M. Widmaier, K. Pfeifer, L. Bommer, V. Presser, *Batteries Supercaps* **2018**, *1*, 11.
[16] S. Fleischmann, A. Tolosa, V. Presser, *Chem. Eur. J.* **2018**, *24*, 12143.
[17] H. S. Choi, J. H. Im, T. Kim, J. H. Park, C. R. Park, *J. Mater. Chem.* **2012**, *22*, 16986.
[18] A. Nugroho, W. Chang, S. J. Kim, K. Y. Chung, J. Kim, *RSC Adv.* **2012**, *2*, 10805.
[19] H. Kim, K.-Y. Park, M.-Y. Cho, M.-H. Kim, J. Hong, S.-K. Jung, K. C. Roh, K. Kang, *ChemElectroChem* **2014**, *1*, 125.
[20] C. Chen, H. Xu, T. Zhou, Z. Guo, L. Chen, M. Yan, L. Mai, P. Hu, S. Cheng, Y. Huang, J. Xie, *Adv. Energy Mater.* **2016**, *6*, 1600322.
[21] L. Cheng, X.-L. Li, H.-J. Liu, H.-M. Xiong, P.-W. Zhang, Y.-Y. Xia, *J. Electrochem. Soc.* **2007**, *154*, A692.
[22] T. Yuan, X. Yu, R. Cai, Y. Zhou, Z. Shao, *J. Power Sources* **2010**, *195*, 4997.
[23] Y.-B. He, F. Ning, B. Li, Q.-S. Song, W. Lv, H. Du, D. Zhai, F. Su, Q.-H. Yang, F. Kang, *J. Power Sources* **2012**, *202*, 253.
[24] H.-G. Jung, S.-T. Myung, C. S. Yoon, S.-B. Son, K. H. Oh, K. Amine, B. Scrosati, Y.-K. Sun, *Energy Environ. Sci.* **2011**, *4*, 1345.
[25] H. Li, L. Shen, X. Zhang, J. Wang, P. Nie, Q. Che, B. Ding, *J. Power Sources* **2013**, *221*, 122.
[26] M. Widmaier, N. Jäckel, M. Zeiger, M. Abuzarli, C. Engel, L. Bommer, V. Presser, *Electrochim. Acta* **2017**, *247*, 1006.
[27] L. Zhao, H.-L. Pan, Y.-S. Hu, H. Li, L.-Q. Chen, *Chin. Phys. B* **2012**, *21*, 028201.
[28] Y. Wang, X. Yu, S. Xu, J. Bai, R. Xiao, Y. S. Hu, H. Li, X. Q. Yang, L. Chen, X. Huang, *Nat. Commun.* **2013**, *4*, 2365.

[29] Y. Sun, L. Zhao, H. Pan, X. Lu, L. Gu, Y.-S. Hu, H. Li, M. Armand, Y. Ikuhara, L. Chen, X. Huang, *Nat. Commun.* **2013**, *4*, 1870.
[30] X. Yu, H. Pan, W. Wan, C. Ma, J. Bai, Q. Meng, S. N. Ehrlich, Y.-S. Hu, X.-Q. Yang, *Nano Lett.* **2013**, *13*, 4721.
[31] K.-T. Kim, C.-Y. Yu, C. S. Yoon, S.-J. Kim, Y.-K. Sun, S.-T. Myung, *Nano Energy* **2015**, *12*, 725.
[32] M. Kitta, R. Kataoka, M. Kohyama, *Phys. Chem. Chem. Phys.* **2016**, *18*, 19888.
[33] X. Feng, H. Zou, H. Xiang, X. Guo, T. Zhou, Y. Wu, W. Xu, P. Yan, C. Wang, J.-G. Zhang, Y. Yu, *ACS Appl. Mater. Interfaces* **2016**, *8*, 16718.
[34] M. Kitta, R. Kataoka, S. Tanaka, N. Takeichi, M. Kohyama, *ACS Appl. Energy Mater.* **2019**, *2*, 4345.
[35] Y. Liu, J. Liu, M. Hou, L. Fan, Y. Wang, Y. Xia, *J. Mater. Chem. A* **2017**, *5*, 10902.
[36] M. Zeiger, N. Jäckel, M. Aslan, D. Weingarth, V. Presser, *Carbon* **2015**, *84*, 584.
[37] M. Zeiger, N. Jäckel, D. Weingarth, V. Presser, *Carbon* **2015**, *94*, 507.
[38] S. Fleischmann, A. Tolosa, M. Zeiger, B. Krüner, N. J. Peter, I. Grobelsek, A. Quade, A. Kruth, V. Presser, *J. Mater. Chem. A* **2017**, *5*, 2792.
[39] N. Jäckel, D. Weingarth, M. Zeiger, M. Aslan, I. Grobelsek, V. Presser, *J. Power Sources* **2014**, *272*, 1122.
[40] K. Pfeifer, S. Arnold, Ö. Budak, X. Luo, V. Presser, H. Ehrenberg, S. Dsoke, *J. Mater. Chem. A* **2020**, *8*, 6092.
[41] D. B. Schuepfer, F. Badaczewski, J. M. Guerra-Castro, D. M. Hofmann, C. Heiliger, B. Smarsly, P. J. Klar, *Carbon* **2020**, *161*, 359.
[42] G. A. Zickler, B. Smarsly, N. Gierlinger, H. Peterlik, O. Paris, *Carbon* **2006**, *44*, 3239.
[43] N. C. Saha, H. G. Tompkins, *J. Appl. Phys.* **1992**, *72*, 3072.
[44] Y. Tang, F. Huang, W. Zhao, Z. Liu, D. Wan, *J. Mater. Chem.* **2012**, *22*, 11257.
[45] C.-K. Lan, S.-I. Chuang, Q. Bao, Y.-T. Liao, J.-G. Duh, *J. Power Sources* **2015**, *275*, 660.
[46] S. Ardizzone, G. Fregonara, S. Trasatti, *Electrochim. Acta* **1990**, *35*, 263.
[47] M. Hillert, *Metall. Trans. A* **1975**, *6*, 5.
[48] M. Opitz, J. Yue, J. Wallauer, B. Smarsly, B. Roling, *Electrochim. Acta* **2015**, *168*, 125.
[49] J. Landesfeind, D. Pritzl, H. A. Gasteiger, *J. Electrochem. Soc.* **2017**, *164*, A1773.
[50] F. J. Günter, J. B. Habedank, D. Schreiner, T. Neuwirth, R. Gilles, G. Reinhart, *J. Electrochem. Soc.* **2018**, *165*, A3249.
[51] E. Kang, Y. S. Jung, G. H. Kim, J. Chun, U. Wiesner, A. C. Dillon, J. K. Kim, J. Lee, *Adv. Funct. Mater.* **2011**, *21*, 4349.
[52] Y. Shi, L. Wen, F. Li, H.-M. Cheng, *J. Power Sources* **2011**, *196*, 8610.
[53] G. Hasegawa, K. Kanamori, T. Kiyomura, H. Kurata, K. Nakanishi, T. Abe, *Adv. Energy Mater.* **2015**, *5*, 1400730.
[54] S. Komaba, T. Ishikawa, N. Yabuuchi, W. Murata, A. Ito, Y. Ohsawa, *ACS Appl. Mater. Interfaces* **2011**, *3*, 4165.
[55] M. Kitta, K. Kuratani, M. Tabuchi, N. Takeichi, T. Akita, T. Kiyobayashi, M. Kohyama, *Electrochim. Acta* **2014**, *148*, 175.
[56] Y. Tian, G. Xu, Z. Wu, J. Zhong, L. Yang, *RSC Adv.* **2017**, *7*, 52702.
[57] K. Pfeifer, S. Arnold, J. Becherer, C. Das, J. Maibach, H. Ehrenberg, S. Dsoke, *ChemSusChem* **2019**, *12*, 3312.
[58] L. Y. Yang, H. Z. Li, J. Liu, S. S. Tang, Y. K. Lu, S. T. Li, J. Min, N. Yan, M. Lei, *J. Mater. Chem.* **2015**, *3*, 24446.